RSC Advances

PAPER

View Article Online
View Journal | View Issue

Cite this: *RSC Adv.*, 2026, **16**, 5064

Preparation and characterization of fish skin gelatin and chitosan-based active dressings for skin wound healing

Jingjing Chen,†[a] Zhide Ruan,†[b] Jikun Pang,†[b] Chuanyan Pan,[b] Haoyu Yang,[c] Xu Luo,[b] Qiyun Qin,[b] Weihao Wei,[b] Guangzheng Jiang,[b] Min Lv*[b] and Huawei Ma *[b]

Skin wound healing remains challenging due to high infection rates and inefficient repair, with traditional dressings lacking mechanical durability and antibacterial control for dynamic wound environments. Herein, an active wound dressing (AWD) was fabricated using fish skin gelatin and chitosan *via* synergistic covalent (MBAA-PNIPAm) and ionic (Ca^{2+}-FSG) crosslinking, integrated with silver nanoparticles (AgNPs), and optimized by finite element modeling. Studies have demonstrated that AWD exhibits outstanding mechanical properties: a tensile strain of 600.05% ± 25.32% and a maximum fracture energy of 2000.47 ± 150.67 J m^{-2}. It also demonstrates efficient thermal responsiveness, with a volume shrinkage rate of 22.17% ± 2.34% at 37 °C over 3 hours. Additionally, it exhibits potent antibacterial activity, achieving an antibacterial rate exceeding 89% against three pathogenic bacteria. Furthermore, it demonstrates excellent biocompatibility, with a cell survival rate exceeding 85% and no significant Ag^{+} accumulation. *In vivo* experiments showed that the wound contraction rate in mice treated with AWD reached 68.67% ± 4.56% within 8 days, significantly promoting granulation tissue formation and epithelial regeneration. The prediction error between the finite element model and experimental results was only 6.61%. This temperature-responsive AWD combines mechanical robustness, antibacterial efficacy, and wound contraction ability, expanding applications of fish-derived gelatin and chitosan. It offers a promising strategy for intelligent trauma repair materials with clinical translation potential.

Received 12th August 2025
Accepted 4th January 2026

DOI: 10.1039/d5ra05902j

rsc.li/rsc-advances

1 Introduction

The difficult healing of skin trauma and the problem of high infection rate pose severe challenges to global public health. According to relevant data, approximately 15% of patients with chronic wounds face the risk of amputation due to secondary infections.[1] Traditional skin trauma treatment methods (such as gauze, cotton wool, *etc.*) alleviate symptoms through passive moisturization and local drug administration, but their defects such as poor mechanical properties and low antibacterial controlled-release efficiency make it difficult to meet the dynamic repair needs of complex wounds.[2] To improve the curative effect of skin trauma, researchers have been focusing on the study of traumatic hemostatic active substances, developing intelligent hemostatic active dressings that respond to physiological signals such as local wound strains, temperature, and pH, realizing self-intelligent regulation of skin trauma and effectively promoting wound healing effects.[3,4] Meanwhile, significant progress has been made in the research of biomimetic adhesive dressings for tissue trauma repair, such as mussel-inspired adhesive dressings,[5] gecko-inspired adhesive dressings,[6] and adhesive dressings based on topological design.[7] Furthermore, hydrogel dressing strategies for external stimuli such as light, ionic strength, glucose, and pH have also been reported,[8] and hydrogels designed through various strategies for cell drug delivery have been developed to promote active wound healing.[9] However, the above-mentioned intelligent hemostatic active dressings generally suffer from problems such as complex manufacturing processes, high costs, drug toxicity and side effects, and difficulties in introducing and controlling the release of active substances, which severely limit their wide application in clinical practice.

Gelatin, as a natural absorbable biomaterial, owes its hemostatic activity to the molecular mechanism of promoting platelet aggregation and coagulation factor release.[10] Currently, gelatin hemostatic sponges derived from bovine or porcine sources have been widely applied in surgical operations.[11] The tilapia (*Oreochromis mossambicus*), as a globally important economic fish, generates by-products such as fish skin and

[a]*Zhejiang Tourism and Health College, Zhoushan Islands New Area, Zhoushan 316000, Zhejiang, China*

[b]*Guangxi Enginerring Research Center of Processing & Storage of Aquatic Products, Guangxi Academy of Fishery Sciences, Nanning 530021, Guangxi, China. E-mail: liaaa2021@126.com; ma463543285@126.com*

[c]*School of Food Engineering, Guangxi Agricultural Engineering Vocational and Technical College, Nanning 530021, Guangxi, China*

† The first authors contributed by Jingjing Cheng, Zhide Ruan, and Jikun Pang.

scales accounting for 20% to 30% of raw materials in its processing industry. Therefore, the effective conversion of fish skin into raw materials for gelatin production can not only achieve efficient resource utilization and alleviate environmental pollution but also create significant economic benefits. However, pure gelatin sponges exhibit disadvantages such as poor mechanical properties and easy breakage. Thus, to obtain high-performance gelatin wound-healing products, it is necessary to carry out composite modification by combining them with other types of healing materials.[4] Studies have shown that chitosan (CS) possesses excellent biocompatibility and biodegradability. CS forms a positive charge barrier at the wound site through amino protonation, inhibiting bacterial adhesion.[12] Its degradation products can activate macrophage M2 polarization, promote angiogenesis, and enhance the healing efficacy.[13]

Studies have reported that embryonic wound healing can seamlessly join wound edges in a zipper-like manner through wound contractile forces and adhesive forces, activating the skin's self-repair mechanism to achieve perfect scarless regeneration of fetal skin.[14,15] Previous approaches for constructing active tissue trauma repair materials mainly involved the following methods: firstly, adding network cross-linked degradable materials to orderly arranged poly (lactic-*co*-glycolic acid) (PLGA) nanofibers to disrupt the microstructures responsible for catalytic functions in hydrogels, using magnetized iron oxide nanoparticle hydrogels;[16] secondly, utilizing ultrasound to break the ionic bonds of ionically cross-linked hydrogels;[17] finally, achieving material activation through photothermal-driven poly(ethylene glycol) diacrylate (PEGDA) hydrogels.[18] However, these methods require external stimuli to drive the activation of active tissue trauma repair materials, and the applied stimuli belong to non-host environments.[19] Currently, there are relatively few research reports on the characteristics of active skin tissue trauma repair materials in the development of active wound dressings.

This study developed an innovative temperature-responsive and mechanically tunable active wound dressing (AWD) for skin trauma healing based on the fish skin gelatin (FSG)-chitosan cross-linked composite system, drawing inspiration from the design concept of strong adhesives.[20] By introducing nano-silver and finite element model optimization technology, this work overcomes the limitations of traditional dressings in terms of cost, processing complexity, and single-functionality. The innovativeness is embodied in three aspects: firstly, combining the thermosensitive property of FSG with the cationic characteristic of chitosan (CS), the "temperature-mechanical" synergistic regulation is used to evaluate its impact on skin regeneration—unlike Ranjbar *et al.* who only prepared hemostatic sponges without thermoresponsive contraction,[11] this work realizes body temperature-triggered wound closure without external devices. Secondly, *in vitro* and *in vivo* experiments are conducted to clarify how the mechanical forces exerted by AWD on skin wounds affect the biological processes of wound healing—compared with Diao *et al.* who used pH/temperature co-response but lacked mechanical mechanism verification,[4] this study links material mechanics to fibroblast behavior (hypothesized *via* TRPV4 activation). Thirdly, the finite element model is employed to optimize and improve the performance of AWD, enabling it to adapt to a broader temperature range—this is the first study to integrate Ogden–Flory theory for quantitative prediction of FSG-CS hydrogel-induced wound contraction, which is not reported in previous literature. The distinctive feature of this study lies in exploring the temperature dependency of AWD contraction, which will be a key focus for future research. Because using AWD in low-temperature environments requires maintaining skin warmth, it is essential to determine whether AWD can also generate contraction in cold-body temperature areas. This study evaluates the tensile properties, matrix toughness, adhesive performance, temperature-sensitive response, antibacterial characteristics, biocompatibility and *in vitro*/*in vivo* wound healing capabilities of AWD. By investigating the contraction ability of AWD under normal body temperature (35–37 °C) and low-temperature conditions, this work provides strong support and scientific evidence for the application of fish skin gelatin and chitosan in skin trauma repair, promoting the development of trauma repair materials toward intelligence and precision.

2 Materials and methods

2.1 Experimental animals

Forty 6-week-old C57BL/6J mice (half male and half female, body weight 20–22 g) were provided by Guangxi Xiaoyanren Biotechnology Co., Ltd (certificate no. SCXK(GX) 2018-0001). The mice had free access to food and water and were maintained under a 12-h light/12-h dark cycle. After a 1-week acclimatization period in the laboratory, they were used for the experiment. Mice were randomly allocated to four groups *via* a random number table (SI Table S1). All evaluators were blinded to the group assignments during wound measurement and histological scoring. Euthanasia was conducted when mice presented with weight loss exceeding 15%, areas of redness and swelling more than twice the wound size, or signs of exhaustion. Given that no significant gender-related differences in wound healing were detected ($p > 0.05$, two-way ANOVA), male and female mice were pooled for statistical analysis.

2.2 Experimental instruments

Polydimethylsiloxane rubber splint (PDSRS), A8BP sterile biopsy punch, TSJ-Q automatic closed tissue dehydrator, BMJ-III tissue embedding machine, MR201 tensile strength tester, and HM315R paraffin microtome were purchased from Guangxi Xiaoyanren Biotechnology Co., Ltd. The MS 400 X UV/vis spectrometer was obtained from Magnettech, Germany, and the 2KBTES-55 freeze dryer was purchased from Shanghai Bioengineering Equipment Company. Field Emission Scanning Electron Microscope (FE-SEM, SU8010, Hitachi, Japan) was used for microstructure observation; Inductively Coupled Plasma Mass Spectrometry (ICP-MS, NexION 350X, PerkinElmer, USA) was used for Ag^+ quantification. Attenuated total reflection Fourier transform infrared (ATR-FTIR) spectrometer (Nicolet iS50, Thermo Fisher Scientific, USA) was used for chemical structure characterization; differential scanning

calorimeter (DSC 250) and thermogravimetric analyzer (TGA 550, TA Instruments, USA) were used for thermal property analysis; electronic balance (ME204E, Mettler Toledo, Switzerland) was used for precise weighing; constant temperature and humidity incubator (HWS-28, Shanghai Yiheng Scientific Instruments Co., Ltd) was used for water vapor transmission rate (WVTR) measurement.

2.3 Experimental materials

Chitosan (CS), *N*,*N*′-methylenebisacrylamide (MBAA), *N*-isopropylacrylamide (NIPAm), calcium sulfate ($CaSO_4$), nano-silver (AgNP, diameter 30 nm), and acrylamide (AAm) were purchased from Guangxi Xiaoyanren Biotechnology Co., Ltd. Hyaluronic acid, 1-(3-dimethylaminopropyl)-3-ethylcarbodiimide (EDC), *N*-hydroxysuccinimide (NHS), ammonium persulfate, tetramethylethylenediamine, and agar plates were obtained from Beijing Bio-Top Technology Co., Ltd. Non-thermosensitive adhesive dressing TA and polydimethylsiloxane were purchased from Beijing Jinclone Biotechnology Co., Ltd. Tilapia skin was provided by Guangxi Luchi Agriculture Co., Ltd. Commercial porcine gelatin sponge (CPGS) and commercial hydrogel dressing (CHD) were used as reference materials for mechanical property comparison. *Staphylococcus aureus* (ATCC 25923), *Pseudomonas aeruginosa* (ATCC 27853), and *Serratia marcescens* (laboratory-preserved) were used for antibacterial tests. Anhydrous calcium chloride (analytical grade, Sinopharm Chemical Reagent Co., Ltd) was used for WVTR measurement; anhydrous ethanol (analytical grade, Xilong Scientific Co., Ltd) was used for porosity determination.

2.4 Experimental methods

2.4.1 Preparation of fish skin gelatin. After 1 kg of fresh tilapia skin was thoroughly washed, it was soaked in 500 mL of 1% NaOH solution for 12 h. The skin was then rinsed with distilled water and placed in 500 mL of 0.6% glacial acetic acid to swell for 3 h. Following another thorough washing, the pH was adjusted to neutral. Gelatin was extracted using the salt extraction method,[21] 15 g of NaCl was dissolved in 500 mL of tap water, and this solution was used to extract gelatin from 1 kg of fish skin at an extraction temperature maintained at 90 °C for 2 h. Finally, the fish skin gelatin was obtained *via* vacuum freeze-drying.

2.4.2 Preparation of AWD. The PNIPAm-FSG with a hybrid network structure, namely AWD, was prepared by covalently cross-linking NIPAm with MBAA, ionically cross-linking FSG with $CaSO_4$, and incorporating AgNP. The detailed preparation method is as follows:

At room temperature, 100 mg of 1.06 M NIPAm and 20 mg of 0.083 M FSG solution were dissolved in 100 mL of phosphate buffer (PBS). Then 60 mg of 0.28 mM MBAA, 50 mg of 0.02 M $CaSO_4$, 45 mg of 0.0065 M ammonium persulfate and 50 mg of 0.0037 M tetramethylethylenediamine were added sequentially. We homogenized the mixture to synthesize the hydrogel precursor in a tissue culture hood, followed by the addition of 4 mg AgNP. We prepared an activator with 20 mg of 2% (w/v) medium molecular weight CS, 12 mg of 12 mg mL^{-1} EDC and 12 mg of 12 mg mL^{-1} NHS. 100 μL of the prepared activator was added to form an adhesive surface on the hydrogel surface. Finally, the mixture was placed in a sealed glass dish and allowed to gel overnight at 4 °C. After gelation, the hydrogel was soaked in saline for 30 min, stored at 4 °C, and rinsed three times before use. The molecular weight of the medium molecular weight CS is 300 000 Da. FSG and CS were subjected to sterile filtration, freezing and lyophilization for 1 week, and all chemical agents were filter-sterilized before use. The schematic diagram of AWD preparation process is shown in SI Fig. S1.

Control experiments were set up as follows: single-network PNIPAm hydrogel (SN) is a hydrogel without $CaSO_4$ for ionic cross-linking of FSG and AgNP; single-network FSG hydrogel (SA) is a hydrogel without MBAA for covalent cross-linking of NIPAm and AgNP; hybrid-network PNIPAm-FSG (OAWD) is AWD without AgNP; room temperature-responsive AWD (AWD-RT) is AWD gelled at 20 °C (close to laboratory room temperature). The PNIPAm-free control group (PF) employed hydrogels synthesized with the identical FSG-CS-AgNP composition as that of the AWD group, yet devoid of PNIPAm, for the purpose of independently assessing the impacts of the temperature-sensitive PNIPAm network. The preparation procedures of AWD-RT, OAWD, SN, SA, and PF all refer to the preparation method of AWD. CPGS and CHD were used as reference materials for mechanical property comparison.

2.4.3 Microstructure characterization. Following freeze-drying, AWD samples were subjected to a 10-nm gold coating through sputtering. Subsequently, these samples were analyzed using field emission scanning electron microscopy (FE-SEM) at an acceleration voltage of 5 kV to investigate pore size and distribution (five samples per group, with five randomly selected fields of view). Samples were prepared as 70-nm ultrathin sections using a microtome. The determination of pore fraction was carried out by means of the ethanol displacement method, where V_1 denotes the volume of ethanol prior to immersion and V_2 represents the volume after immersion.

$$\text{Pore fraction} = (V_1 - V_2)/V_1 \times 100\% \quad (1)$$

2.4.4 Shear test. The unidirectional strength of samples (80 mm × 5 mm × 1.5 mm) was measured using a tensile strength tester (with a maximum load capacity of 50 N). Mechanical testing conditions: samples were fully hydrated in PBS (4 °C, 24 h) before testing; gauge length 30 mm; strain rate 5 mm min^{-1}; temperature 4 °C (controlled by a thermostatic chamber); strain was measured by the tester's built-in displacement sensor. The tensile ultimate strength was defined as the ratio of the tensile strength at sample fracture to that of the initial undeformed sample. The elastic modulus was calculated as the tangent of the small strain region (<10%) on the stress–strain curve, and the fracture energy was determined based on the stress–strain curves of undamaged and damaged samples. SA, SN, OAWD, AWD-RT, PF, CPGS, and CHD were set as control groups to measure shear stress. A unidirectional shear force was applied at a constant rate of 5 mm min^{-1} to observe the inflection point between the elastic stage (strain <

10%) and the plastic stage. For evaluating matrix toughness, an additional group of AWD prepared with 2 M NIPAm (2M-AWD) was included. All mechanical tests were repeated 5 times; data were presented as mean ± SD, and statistical analysis was performed by one-way ANOVA with Tukey's post-hoc test ($p < 0.05$).

2.4.5 Peel adhesion test. A tensile strength tester was used to perform 180° peel tests on AWD for evaluating its adhesive properties, with 6-week-old C57BL/6J mice as experimental subjects (gender differences were ignored). AWD and control groups (SA, SN, OAWD, PF, non-thermosensitive TA, traditional medical bandage (Band-Aid) were cut into rectangular specimens (80 mm × 5 mm × 1.5 mm). One end of each specimen was fixed to a mouse skin model (1.5 mm thickness), and the other end was secured using a fixture. The experiment was conducted under standard conditions (peel rate: 100 mm min^{-1}). Ultimate tensile strain was defined as the percentage of maximum elongation before fracture. For peel tests, fresh mouse dorsal skin (24 h post-mortem) was used to ensure consistent tissue properties, and each group was tested in triplicate. After removing outliers, the mean value was calculated. The adhesive energy was calculated using the following formula, where F_{max} represents the maximum stable force (N) during peeling, and W denotes the specimen width (mm).

$$\text{Adhesive energy} = 2 \times F_{max}/W \quad (2)$$

2.4.6 Thermosensitive response characterization. The thermosensitive response of AWD was quantitatively characterized by volume change. AWD samples with different acrylamide (AAm) contents (0%, 1%, and 5% AAm, referring to the molar percentage of AAm in the total monomers (AAm + NIPAm)) and control groups (SA, SN, OAWD, PF) were cut into circular discs with a diameter of 10 mm and thickness of 1.5 mm. These discs were placed in 37 °C phosphate buffered saline (PBS), and their volume changes were recorded at different time points. ImageJ software was used for image analysis. At time points 0, 0.5, 1, 2, 3, 4, 6, and 8 hours, the sample photos were measured with a calibration ruler, and the volume was calculated according to formula (2), where r is the radius and h is the thickness. The experiment was conducted in a thermostatic chamber (±0.5 °C), with each group repeated three times. The data were averaged after excluding outliers. The volume shrinkage rate (S_A) was calculated using the following formula, where V_0 and V_1 represent the initial volume and final volume.

$$V = \pi r^2 h \quad (3)$$

$$S_A = 1 - (V_0/V_1) \quad (4)$$

Data were presented as mean ± SD; statistical analysis was performed by two-way ANOVA (factors: time, AAm content) with Tukey's post-hoc test ($p < 0.05$).

2.4.7 Antibacterial properties. Following the antibacterial test protocol for contact wound dressings,[22] the experiment utilized laboratory-cultured strains of *Serratia marcescens*, *Staphylococcus aureus* (ATCC 25923), and *Pseudomonas aeruginosa* (ATCC 27853). The bacterial strains were incubated in LB broth at 37 °C for 12 hours at 180 rpm, with the final concentration adjusted to 1×10^6 CFU per mL by colony-forming unit (CFU) enumeration. Two experimental groups were established: the OAWD group (AWD without AgNP) and the AWD group (AWD containing AgNP), with the PF group and CHD as additional controls. A 100 μL bacterial suspension was applied to the surface of AWD/OAWD/PF/CHD (10 mm diameter, 1.5 mm thickness) with a contact area of 0.785 cm^2. After 24-hour incubation at 37 °C, the dressings were transferred to 5 mL PBS buffer and vortexed for 10 minutes to elute bacteria. The eluate was then serially diluted (10^{-1} to 10^{-5}). 100 μL of each diluted bacterial suspension was plated on LB agar plates, incubated at 37 °C for 24 hours, and CFU counts were performed. The antibacterial rate was calculated using the following formula, where CFU_0 represents the absence of dressings:

$$\text{Antibacterial rate} = (CFU_0 - CFU_1)/CFU_0 \times 100\% = 0 \quad (5)$$

2.4.8 AgNP release profile and tissue Ag^+ quantification. The release profiles of silver species (AgNP and Ag^+) from AWD were explored by integrating UV/vis spectroscopy and ICP-MS. Standardized rectangular AWD specimens (15 mm × 10 mm × 1.5 mm) were cut and immersed in 1 mL of DPBS in sterile centrifuge tubes. Then, the tubes were put in a 37 ± 0.5 °C constant-temperature incubator to mimic the human physiological environment. The DPBS supernatant was collected, replaced at set time points (0.5 h, 1 h, 2 h, 8 h, 24 h, 48 h, and 7 d), and stored at 4 °C for subsequent detection. For AgNP detection, a UV/vis spectrometer (MS 400×) was used at 420 nm. A calibration curve was established with gradient-concentration standard AgNP solutions (0.03125, 0.0625, 0.125, 0.25, 0.5, and 1 mg mL^{-1}), and the AgNP concentration in the release medium was calculated by substituting absorbance values into the curve equation. For total Ag and Ag^+ detection *via* ICP-MS (NexION 350X), the release medium was directly analyzed for total Ag based on a pre-established Ag standard curve (0.1–10 μg mL^{-1}). For Ag^+ determination, the medium was filtered through a 3 kDa ultrafiltration membrane, and the filtrate was analyzed by ICP-MS. The cumulative release amount of silver species was calculated using a formula.

$$\text{Cumulative release} = \sum (C_t \times V)/S \quad (6)$$

where C_t is the detected concentration of target silver species (AgNP, total Ag, or Ag^+) at time t (μg mL^{-1}), V is the volume of DPBS (1 mL), and S is the surface area of AWD (1.5 cm^2). To determine total Ag content in AWD, fresh AWD specimens without release treatment were digested with a 3 : 1 HNO_3–H_2O_2 mixed solution at 95 °C until dissolved, diluted with ultrapure water, and analyzed by ICP-MS, with the content normalized by AWD surface area (μg cm^{-2}). For Ag^+ detection in mouse tissues, mice were euthanized 8 days after AWD treatment, and wound-site skin, liver, and kidney tissues were collected. The tissues were digested with the same 3 : 1 HNO_3–H_2O_2 solution at 95 °C, diluted, and analyzed by ICP-MS to quantify Ag^+. All detection

experiments were triplicated, with results as mean ± SD. The Ag^+ concentration in mouse tissues was statistically analyzed by *t*-test against the control group, and a $p < 0.05$ was significant to ensure data reliability and reproducibility.

2.4.9 Cytotoxicity test on fibroblasts/keratinocytes. Mouse embryonic fibroblasts (NIH/3T3, purchased from China General Microbiological Culture Collection Center, CGMCC, catalog no. GDC0073) and human keratinocytes (HaCaT, purchased from China General Microbiological Culture Collection Center, CGMCC, catalog no. GDC0151) were obtained from CGMCC. Cells were seeded in 96-well plates at 1×10^4 cells per well in DMEM medium containing 10% fetal bovine serum (FBS) and 1% penicillin–streptomycin. The cells were incubated at 37 °C with 5% CO_2 for 24 hours. AWD extract was then added at dilution ratios of 10%, 25%, 50%, and 100% to the medium, followed by incubation for another 24 hours. CCK-8 reagent (10 μL per well) was added, and absorbance was measured at 450 nm. The cell viability was calculated using the following formula:

$$\text{Cell viability} = \frac{OD_n - OD_0}{OD_1 - OD_0} \times 100\% \quad (7)$$

OD_n denotes the absorbance of the experimental group; OD_1 indicates the absorbance of the normal cell group; OD_0 represents the absorbance of the control group containing only DMEM Complete Medium + CCK-8 without cells, used to correct for reagent background absorption.

2.4.10 *In vitro* wound healing assay. Six-week-old mice were selected as experimental subjects. A sterile scalpel was used to incise the dorsal skin, creating a wound with a diameter of 10 mm on the incised skin. AWD (15 mm × 15 mm × 1.5 mm) and control dressings (TA, PF, CHD) were placed over the wound and gently pressed for 15 min at room temperature. After treatment, the skin samples together with AWD were incubated at 37 °C for 2 days. The samples were then removed, subjected to freezing treatment in liquid nitrogen, and AWD was removed to measure the wound size. The experiment included an AWD group, the TA group (using the non-thermosensitive dressing TA), the PF group (PNIPAm-free control), the CHD group, and the CG group (non-treatment control group). Wound size was measured by ImageJ software (mean ± SD, $n = 5$). Statistical analysis: one-way ANOVA with Tukey's post-hoc test ($p < 0.05$). The wound contraction rate was computed using the following formula: where W_0 representing the initial wound size divided by W_t representing the wound size at 2 days.

$$\text{Wound contraction ratio} = (W_0 - W_t)/W_0 \times 100\% \quad (8)$$

2.4.11 *In vivo* experiments. Six-week-old mice were anesthetized with 4% isoflurane, and subsequently, 1% isoflurane was continuously administered to sustain anesthesia. The dorsal skin was shaved, and residual hair was eliminated using depilatory cream. A full-thickness skin defect with a diameter of 0.5 centimeter was generated on the dorsal region using an A8BP biopsy punch. To preclude spontaneous wound closure, an annular hollow polydimethylsiloxane rubber splint (PDSRS) was centered over the wound and fixed with cyanoacrylate adhesive. An AWD with a diameter of 0.55 centimeter was placed within the splint and compressed onto the wound using a cryogenic spray gun for 2 minutes. The dressing was then covered with Tegaderm and a bandage to prevent dehydration and mechanical interference. After recovery from anesthesia, mice were returned to their cages and monitored daily for health status. Dressings and surrounding tissues were harvested on days 3 and 8 for histological analysis. A non-thermosensitive dressing group (TA), a PNIPAm-free control group (PF), a CHD group, and a blank control group (CG) were included to ensure experimental rigor and reproducibility.

2.4.12 Skin histological evaluation. Skin tissue samples collected from *in vivo* experiments were fixed in PBS containing 4% paraformaldehyde and stored at 4 °C overnight, followed by three rinses with PBS to remove excess fixative. Tissues were sectioned (5 μm thickness), stained with hematoxylin and eosin (H&E), and observed under a biological microscope. Blind evaluation was performed by two independent pathologists using a four-point scoring system for inflammation, and granulation tissue formation. The histopathological scoring criteria for wound healing are shown in SI Table S2. Data are presented as the mean ± standard deviation (SD). Statistical analysis was conducted using one-way analysis of variance (ANOVA) followed by Tukey's post-hoc test, with statistical significance set at $p < 0.05$.

2.4.13 Finite element simulation. Finite element simulations were performed using ABAQUS version 2017 software, incorporating a user-defined subroutine module (UHYPER subroutine) to model the thermoresponsive behavior of AWD. The nonlinear thermoresponse of AWD was implemented using the free energy function of the modified Flory–Rehner model within the ABAQUS UHYPER subroutine. An Ogden elastic model for skin was constructed based on relevant equations. AWD thermoresponsiveness, modified Flory–Rehner model free energy function $F = F_{mix} + F_{elastic} + F_{thermal}$; $\chi = 0.52$, $N = 1000$, $\rho = 1.05$ g cm^{-3} (SI Table S3).

$$s = \mu(\lambda\alpha - \mu\alpha/2) \quad (9)$$

where λ is the stretch ratio, α and μ are Ogden coefficients (10 Pa and 110 Pa, respectively), and s denotes nominal stress. Nominal stress refers to the overall equivalent stress, rather than the local force acting on the structure, defined as the stress of the tested sample divided by the cross-sectional area of the undeformed sample. The constants α and μ were obtained by fitting the stress–stretch curve of mouse skin, with the fitting coefficients valid for stretch ratios less than 1.6. When λ exceeds 1.6, the stress–stretch curve becomes serrated, indicating rupture or wound debonding.

$$G = E/2(1 - V) \quad (10)$$

The shear modulus (G) of AWD was determined using eqn (10), where E is the elastic modulus measured from tensile tests, and V denotes Poisson's ratio (0.5). During simulation, a 2D

system was constructed for the symmetric AWD and skin using eight-node quadratic plane stress quadrilateral hybrid elements. The mouse skin was modeled with a width of 100 mm, while the AWD and wound widths were set to 8 mm and 4 mm, respectively. The left and right edges of the skin were fully constrained, and the bottom edge was fixed in the horizontal direction. The temperature range triggering the active response of AWD was set to 280–310 K. The skin thickness was 0.5 mm, and variations in the thickness, width, and shear modulus of AWD were monitored.

$$R = 1 - (w/W)^2 \quad (11)$$

Eqn (11) defines the wound contraction ratio (R), where w and W represent the wound size (mm) before and after contraction, respectively.

2.4.14 Data processing. Data were presented as mean ± standard deviation, finite element simulations were performed using ABAQUS version 2017, statistical analyses were conducted with Origin 2024, one-way ANOVA with Tukey's post-hoc test was used for multi-group comparisons (mechanical properties, wound contraction, histological scores), two-way ANOVA with Tukey's post-hoc test for time-dressing interactions (Ag^+ release, thermosensitive volume change), and independent samples t-test for pairwise comparisons (tissue Ag^+ concentration). Statistical significance was defined as $p \leq 0.05$.

3 Results

3.1 Tensile properties

Cryogelation and the ordered arrangement of gelatin molecular chains promote the formation of a porous network structure, which endows the hydrogel with uniform architecture, high stretchability, porosity, and superior toughnes.[23] As depicted in Fig. 1a, the stress–strain curve of AWD displays a notably larger extension range in comparison to groups such as SA, SN, and AWD-RT. In conjunction with Fig. 1b, the tensile strain of AWD is 600.05% ± 25.32%, which is significantly higher than that of SN (280.12% ± 18.45%), AWD-RT (250.67% ± 20.11%), and PF (320.45% ± 22.68%) ($p < 0.05$), suggesting that AWD demonstrates remarkably superior tensile extensibility and structural robustness compared to the other tested dressings. Moreover, the dispersion state of silver nanoparticles (AgNP) in AWD was characterized *via* UV-vis spectroscopy, relying on the shape and broadening of characteristic absorption peaks. As shown in SI Fig. S2, AWD presents a single, symmetric characteristic absorption peak at 420 nm without peak broadening, indicating that the AgNP in AWD are non-aggregated and well-dispersed.

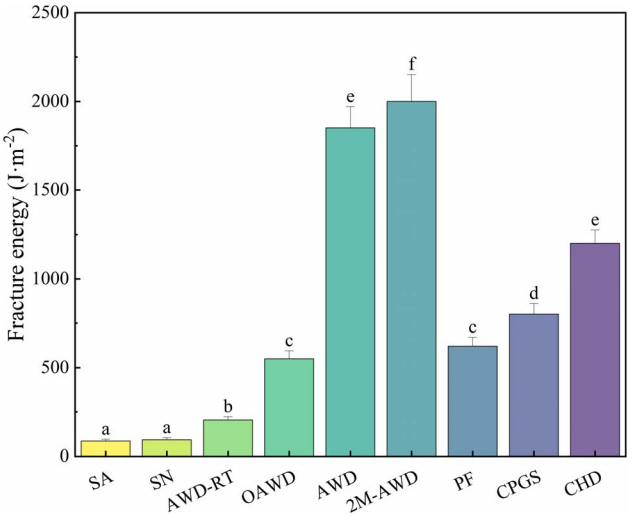

Fig. 2 Comparison of matrix toughness of various hydrogel matrices. Different letters indicate significant differences between groups.

3.2 Matrix toughness

Matrix toughness, a critical indicator for measuring a material's resistance to deformation and fracture, is such that an increase in its value significantly enhances the mechanical properties of the

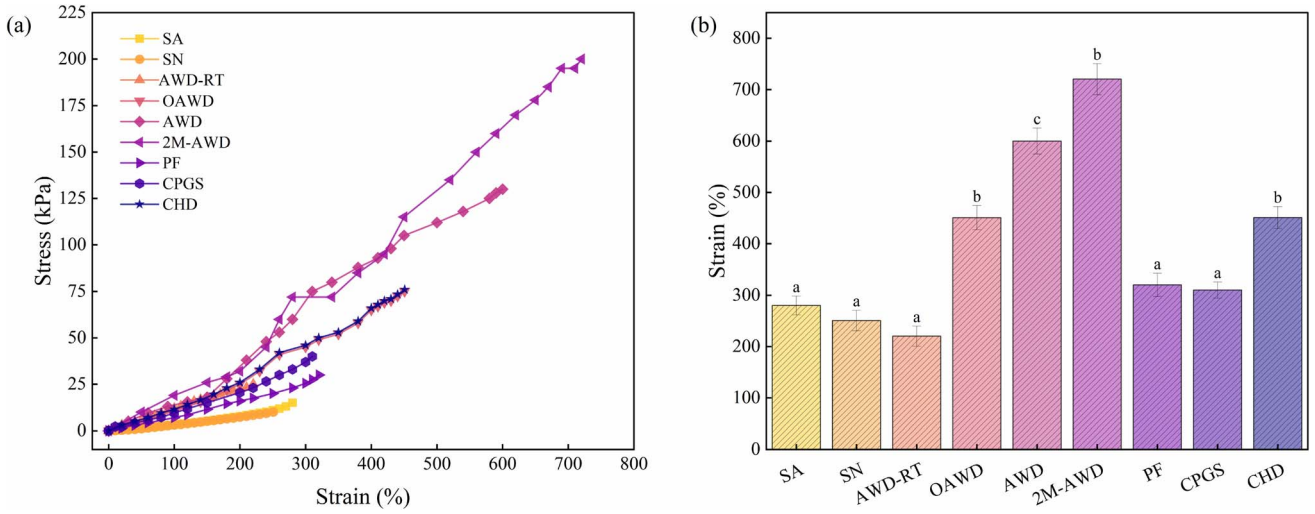

Fig. 1 Stress–strain curves (a) and tensile strain comparison (b) of AWD and control dressings (SA, SN, AWD-RT, OAWD, 2M-AWD, PF, CPGS, CHD) at 4 °C.

material.[24] The quantitative analysis results based on shear tests are shown in Fig. 2. The fracture energy of OAWD is 550.12 J m^{-2}, significantly higher than that of AWD-RT prepared at 20 °C (204.27 J m^{-2}). In contrast, both single-network systems SA and SN exhibit fracture energies below 100 J m^{-2}. The fracture energy of AWD was 1850.67 ± 120.45 J m^{-2}, which was significantly higher than of OAWD (550.12 ± 45.32 J m^{-2}), PF (620.89 ± 50.11 J m^{-2}), commercial porcine gelatin sponge (800.34 ± 60.23 J m^{-2}), and commercial hydrogel dressing (1200.56 ± 75.45 J m^{-2}) ($p < 0.05$). The addition of AgNP had no significant effect on the matrix toughness of AWD ($p > 0.05$), while increasing the NIPAm monomer concentration to 2 M enhanced the fracture energy of 2 M-AWD to 2000.47 ± 150.67 J m^{-2}. Additionally, phase separation between PNIPAm and FSG was observed at room temperature, which we speculate is associated with the lower hydrophilicity of NIPAm compared to acrylamide, whereas low temperature environments safeguard the homogeneity of the hybrid network by suppressing phase separation tendencies.[25]

3.3 Structural characterization

Field emission scanning electron microscopy (FE-SEM) was additionally utilized to characterize the microstructural features of the dressings. Statistical analyses of pore size, pore density, and the coefficient of variation (CV) were conducted to assess the uniformity of pore distribution (SI Table S4). The pore distribution range of AWD (SI Fig. S3a) was 50–80 μm, whereas that of OAWD (SI Fig. S3b) was 70–100 μm. AWD presented a more regular pore morphology. The corresponding pore structure parameters indicated that AWD had an average pore size of 65 ± 8 μm, a pore density of 28 ± 3 pores/100 μm^2, and a CV of 0.18. In contrast, OAWD had an average pore size of 85 ± 12 μm, a pore density of 19 ± 2 pores/100 μm^2, and a CV of 0.25. These findings suggest that AWD possesses a more uniform porous structure and a higher pore density.

To clarify the chemical structural characteristics of AWD, Fourier Transform Infrared (FTIR) spectroscopy was employed to analyze the functional groups of AWD, OAWD, PNIPAm, CS, and FSG. The types of cross-linking were determined by the shifts, additions, or broadening of characteristic peaks. As depicted in SI Fig. S4, FSG, CS, and PNIPAm displayed their respective characteristic functional group peaks. Compared with the pure components, the FTIR spectra of AWD exhibited three crucial changes: the shift of the amide I band of PNIPAm (1655 cm^{-1}) to 1648 cm^{-1}, the emergence of a Ca–O stretching vibration peak at 1030 cm^{-1}, and the broadening of the N–H stretching vibration peak at 3280 cm^{-1}. These results imply that AWD successfully constructed a hybrid network structure with covalent-ion-hydrogen bond synergistic cross-linking. Experimental results demonstrated that the regulation of the network structure of FSG through cryogelation at 4 °C promoted the uniform cross-linking of the FSG-CS hybrid network, thereby synergistically enhancing the extensibility and toughness of AWD.

3.4 Adhesive properties

Adhesion energy, a key parameter for evaluating the interfacial bonding strength between wound repair materials and tissues, is such that an increase in this value significantly enhances the functional durability of materials in dynamic physiological environments.[5] Quantitative analysis *via* standard 180° peel tests, revealed that hybrid network-structured AWD and OAWD exhibited significantly higher adhesion energies than single-network SA (15.09 J m^{-2}), SN (17.22 J m^{-2}), non-thermosensitive TA (22.37 J m^{-2}), and traditional medical bandage Band-Aid (10 J m^{-2}) (Fig. 3a), indicating their remarkable advantages in tissue adhesion. AWD showed an adhesion energy of 173.85 ± 12.67 J m^{-2}, which was 38.5% higher than OAWD (125.64 ± 9.89 J m^{-2}), 2.1-fold higher than PF (82.34 ± 7.56 J m^{-2}), and 3.5-fold higher than CHD (49.87 ± 5.34 J m^{-2}) ($p < 0.05$) (Fig. 3a). Additionally, AWD containing AgNP showed an adhesion energy of 173.85 J m^{-2}, representing a 38.5% increase compared to AgNP-free OAWD (125.64 J m^{-2}) (Fig. 3b), demonstrating that the incorporation of AgNP further optimizes interfacial adhesion. This phenomenon is primarily attributed to AgNP acting as nanoparticles, which enhance the flexibility of gelatin molecular chains through a hydration effect and promote the adhesive properties of gelatin.[16,26]

3.5 Water vapor transmission rate (WVTR)

For the testing method, the WVTR was calculated by weighing the change in the mass of the moisture permeation cup before and after testing, in accordance with the ASTM E96-00 standard (cup method). The test results are shown in SI Table S5. The WVTR value of AWD was 2652.38 ± 58.45 g $(m^2\ 24\ h)^{-1}$, which falls within the ideal WVTR range for wound healing (2000–3000 g $(m^2\ 24\ h)^{-1}$) and is significantly higher than that of CHD (1856.24 ± 42.56 g $(m^2\ 24\ h)^{-1}$) ($p < 0.05$). The results indicate that AWD not only effectively evaporates excess exudate from the wound surface, prevents wound maceration and bacterial growth, but also maintains adequate humidity to sustain wound moisture. Both the OAWD group and PF group exhibited higher WVTR values than the AWD group, which may be attributed to the lack of AgNP and PNIPAm.

3.6 Antibacterial properties

Owing to their unique surface plasmon resonance effect and quantum confinement properties, AgNP exhibit excellent nanoscale antibacterial activity.[27] This study systematically evaluated the antibacterial performance of AWD and OAWD. The experimental results are shown in Fig. 4. For *Serratia marcescens*, the antibacterial rate of the AWD group was 92.03% ± 3.48%, significantly higher than that of the OAWD group (8.19% ± 1.51%), PF group (18.94% ± 3.09%), and CHD group (35.24% ± 4.19%) ($p < 0.05$). For *Staphylococcus aureus*, the AWD group achieved a remarkable 90.13% ± 3.52% antibacterial efficacy, significantly outperforming the OAWD group (15.62% ± 2.81%), PF group (18.92% ± 3.13%), and CHD group (35.19% ± 4.21%) ($p < 0.05$). In the case of *Pseudomonas aeruginosa*, the AWD group demonstrated 89.47% ± 4.11% antibacterial efficacy, showing significant improvement over the OAWD group (12.31% ± 2.52%), PF group (14.74% ± 3.03%), and CHD group (32.15% ± 3.81%) ($p < 0.05$). The results showed that the antibacterial rate of AWD was significantly higher than of other

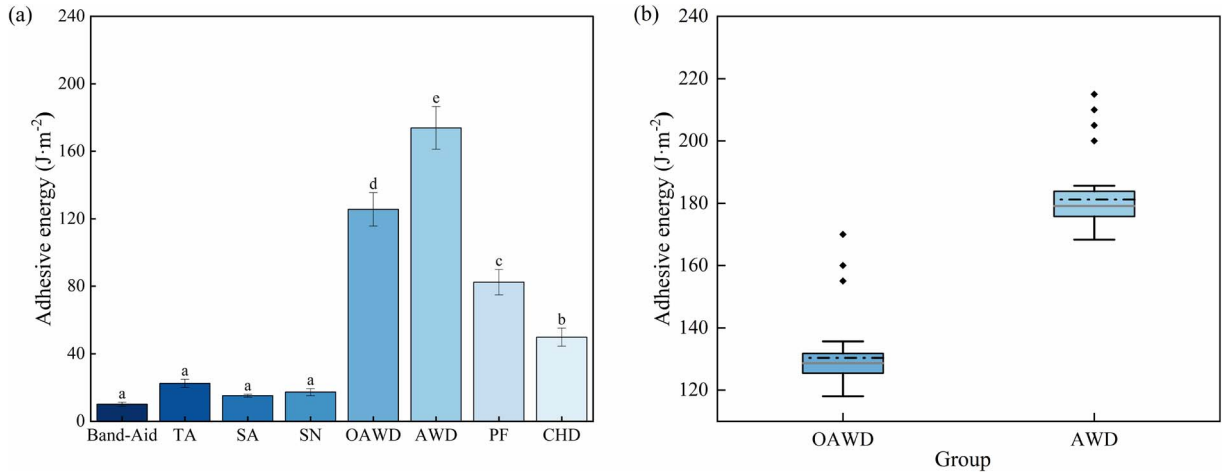

Fig. 3 Comparison of adhesiveness of various hydrogel matrices. Among them, (a) represents the comparison of the adhesive energy of different types of wound repair materials (Band-Aid, TA, SA, SN, OAWD, AWD, PF, CHD); (b) represents the adhesive energy data of the OAWD group without AgNP and the AWD group with AgNP. Different letters indicate significant differences between groups.

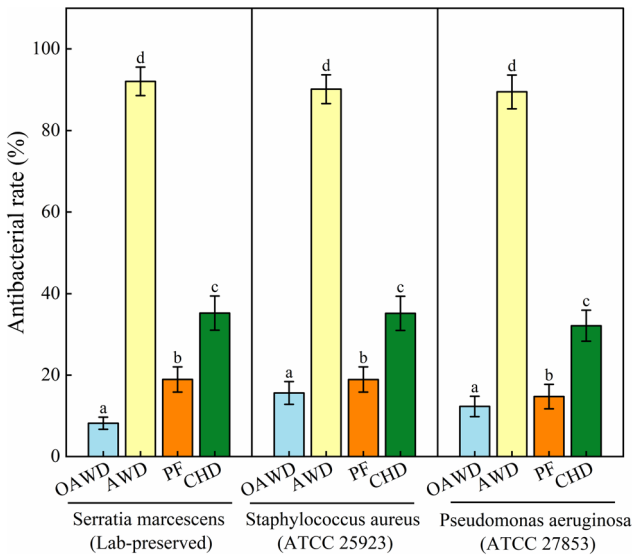

Fig. 4 Comparison of antibacterial functions among different hydrogels. Different letters indicate significant differences between groups.

dressings for all three strains, indicating that AWD could significantly inhibit bacterial growth.

A release experiment was conducted to investigate whether AgNP content decreases over time. UV/vis results showed no AgNP leakage absorbance at 420 nm < 0.01, while ICP-MS results showed sustained Ag^+ release. Cumulative Ag^+ release at 7 d was 15.67 ± 1.23 μg cm^{-2}, with a release rate of about 0.95 μg cm^{-2} d^{-1}. Total Ag content per AWD was 25.34 ± 2.11 μg (SI Table S6)., revealing no AgNP leakage from AWD and suggesting that its antibacterial function relies on Ag^+ release.

3.7 Biocompatibility

3.7.1 Host cell cytotoxicity. Mouse embryonic fibroblasts (NIH/3T3) and human keratinocytes (HaCaT) were used to evaluate AWD's cytotoxicity. AWD extract (10–100% v/v) showed no significant toxicity: 100% extract concentration resulted in 88.53% ± 4.21% viability for NIH/3T3 cells and 86.13% ± 3.82% viability for HaCaT cells, which was not significantly different from the control group ($p > 0.05$) (SI Table S7). Low extract concentrations (10–50%) showed >95% cell viability, confirming that AWD does not damage skin repair-related cells.

3.7.2 Tissue Ag^+ accumulation. ICP-MS analysis of mouse tissues (8 d post-treatment) showed no significant Ag^+ accumulation in AWD group: wound skin (0.89 ± 0.12 μg g^{-1}), liver (0.34 ± 0.05 μg g^{-1}), kidney (0.28 ± 0.04 μg g^{-1}), which was comparable to CG group ($p > 0.05$, SI Table S8). This indicates that AWD's Ag^+ release does not cause systemic toxicity.

3.8 DSC/TGA

The DSC curves are shown in SI Fig. S5a. AWD exhibits a single endothermic peak at 32.5 ± 0.8 °C, which corresponds to the lower critical solution temperature (LCST) of the PNIPAm network. This temperature is slightly below the human physiological temperature (37 °C), ensuring that AWD can rapidly respond to body temperature and undergo phase transition contraction upon wound contact, thereby providing mechanical driving force for wound contraction. As a control, the PF group without PNIPAm showed no significant endothermic peak within the 0–80 °C range, confirming that the thermosensitive response of AWD originates from the PNIPAm network.

The thermogravimetric analysis (TGA) curves are shown in SI Fig. S5b. The thermal decomposition process of AWD is divided into three stages: the first stage (30–100 °C) involves water evaporation in both groups, with residual masses of 92.2% (AWD) and 92.5% (PF) respectively, showing minimal difference due to similar moisture content. Weight loss during this stage is unrelated to PNIPAm. The second stage (100–280 °C) exhibits more significant weight loss in the AWD group, with a residual mass of 67.7%. The third stage (280–600 °C) is dominated by main-chain thermal degradation in both groups, accounting for

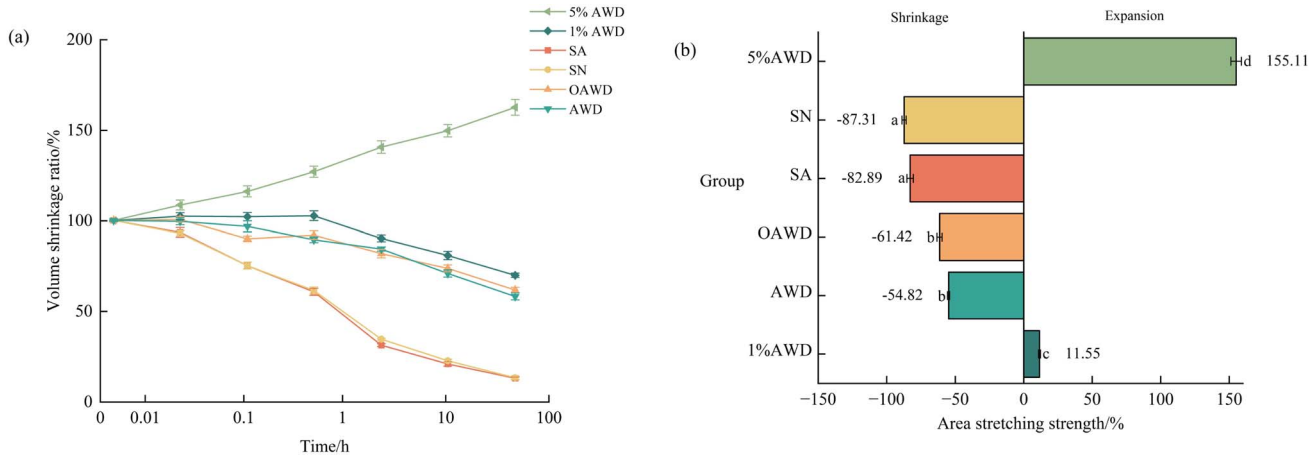

Fig. 5 Temperature triggering changes in volume and area of various hydrogels. (a) Shows the variation trends of the volume shrinkage rates of different types of wound repair materials (5% AWD, 1% AWD, SN, SA, OAWD, AWD) with time. (b) Presents the area stretching strength data of different material groups (5% AWD, SN, SA, OAWD, AWD, 1% AWD). Among them, a negative value of area strain indicates shrinkage, and a positive value indicates expansion. The 1% and 5% addition amounts refer to 1% and 5% of the acrylamide content in the total monomers, respectively. Different letters indicate significant differences between groups.

the largest weight loss. After 600 °C, the residual masses of both groups stabilize without significant weight loss, indicating complete degradation of the organic phase with only inorganic filler remaining.

3.9 Swelling ratio

SI Fig. S6 shows the swelling kinetics curves of AWD at 25 °C and 37 °C. At 25 °C (below the LCST), the swelling rate increased continuously over time and was significantly higher than of other groups ($p < 0.05$); the OAWD group and PF group exhibited swelling rates close to but lower than of the AWD group, while the CHD group showed the lowest swelling rate with slow growth. At 37 °C (above the minimum critical dissolution temperature), the AWD group reached a peak swelling rate of 225.71 ± 6.81% at 2 h, after which the swelling rate continued to decline, reaching 110.23 ± 5.21% at 24 h. The OAWD group and PF group showed sustained increases in swelling rate over time, consistent with the trend at 25 °C; the CHD group exhibited a steady and slow increase in swelling rate.

3.10 Temperature-responsive triggering of skin contraction

This study was based on the hypothesis that AAm can regulate the contraction behavior of AWD, investigating the temperature-triggered contraction of adhesive hydrogels and the modulation of their thermosensitivity by AAm addition. The temperature-induced volume shrinkage and areal strain of the skin-mimicking model were studied, where results indicated that AWD exhibits significant temperature-triggered contraction at 37 °C. AWD volume shrinkage at 3 h was 22.17% ± 2.34%, significantly higher than of PF (3.56% ± 0.89%), SA (2.12% ± 0.67%), and SN (1.89% ± 0.54%) ($p < 0.05$). Areal contraction tension of AWD was 54.82% ± 4.56%, significantly higher than that of PF (4.23% ± 0.98%) ($p < 0.05$) (Fig. 5a and SI Table S9). SI Fig. S7 shows representative images of AWD before (A) and after (B) 37 °C treatment, with clear volume shrinkage observed. Further observations revealed that the areal contraction tension varied with the relative contents of AAm and NIPAm, such that increasing AAm loading from 1% to 5% induced a polarity reversal from contraction to expansion; the 5% AWD group showed an 11.67-fold higher expansion than the 1% group (Fig. 5b). This significant change indicated that the thermosensitive components in the 5% AWD underwent a drastic phase transition under the action of temperature, inducing strong self-swelling of the material, thereby providing a powerful mechanical impetus for triggering skin expansion. Compared to mussel-mimetic, gecko-mimetic, and topology-designed adhesive dressings,[5–7] AWD exhibited superior mechanical adaptability and dynamic responsiveness in its contraction behavior.

3.11 *In vitro* wound contraction performance of AWD on mouse skin

Wound size on mouse skin was measured to characterize the *in vitro* wound contraction capability of AWD, presenting observation results from five groups (Fig. 6 and SI Table S10): the AWD group (containing AgNP), non-treatment control group (CG), non-thermosensitive dressing (TA) group, PF group (PNIPAm-free control), and CHD group. Results showed that the wound contraction ratio of the CG group remained at a low level of only 2.01% ± 0.56%, reflecting limited natural wound contraction in the absence of intervention, while the TA group exhibited an increased contraction ratio of 8.07% ± 1.23% that still lagged significantly behind that of the AWD group. The AWD group demonstrated a wound contraction ratio of 50.12% ± 4.89%, which was significantly higher than those of CG (2.01% ± 0.56%), TA (8.07% ± 1.23%), PF (15.34% ± 2.11%), and CHD (22.56% ± 3.45%) ($p < 0.05$).

This robust contraction ability may be attributed to structural changes within AWD at 37 °C, which induce a contraction effect on the covered wound to exert contractile forces on wound edges—mechanical stimulation that may promote collagen

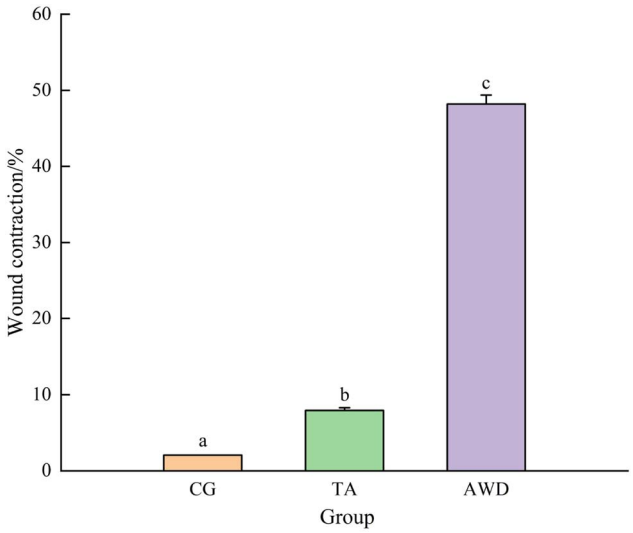

Fig. 6 Comparison of wound contraction ability of different materials *in vitro*. Different letters indicate significant differences between groups.

orientation by activating fibroblast TRPV4 ion channels (this is a hypothesis to be verified in future studies)—thereby facilitating wound healing.[28,29] SI Fig. S8 shows the hypothesized mechanism of AWD-induced wound healing *via* TRPV4 activation.

3.12 *In vivo* wound contraction performance of AWD on mouse skin

A mouse skin wound model was employed to mimic the natural healing process of human and mammalian skin wounds with enhanced precision by restricting the normal wound contraction process.[30] Quantitative analysis of wound contraction ratios over different time points was conducted *via* continuous observation of wound healing in mice, including five groups: non-treatment control (CG), non-thermosensitive dressing (TA), AWD (temperature-responsive, AgNP-loaded), PNIPAm-free control (PF), and CHD. At Day 3, the AWD group exhibited a significantly higher contraction ratio (40.34% ± 3.89%) compared to TA (12.56% ± 2.34%), PF (18.78% ± 3.11%), CHD (25.12% ± 3.56%), and CG (8.97% ± 1.89%) (all $p < 0.05$). By Day 8, the contraction ratio of the AWD group further increased to 68.67% ± 4.56%, which remained substantially higher than the values of TA (22.13% ± 3.01%), PF (30.45% ± 3.78%), CHD (38.97% ± 4.23%), and CG (40.05% ± 4.89%) (all $p < 0.05$) (Fig. 7a and SI Table S7). These results confirm that AWD sustains efficient promotion of wound contraction throughout the entire observation period.

Histological staining of wound tissues on Day 8 (Fig. 7b and SI Table S11) revealed that the AWD-treated group had abundant, orderly arranged fibroblasts, reduced inflammatory cell infiltration, and continuous epithelial coverage (≥70% of the wound area). In contrast, the TA and CG groups showed

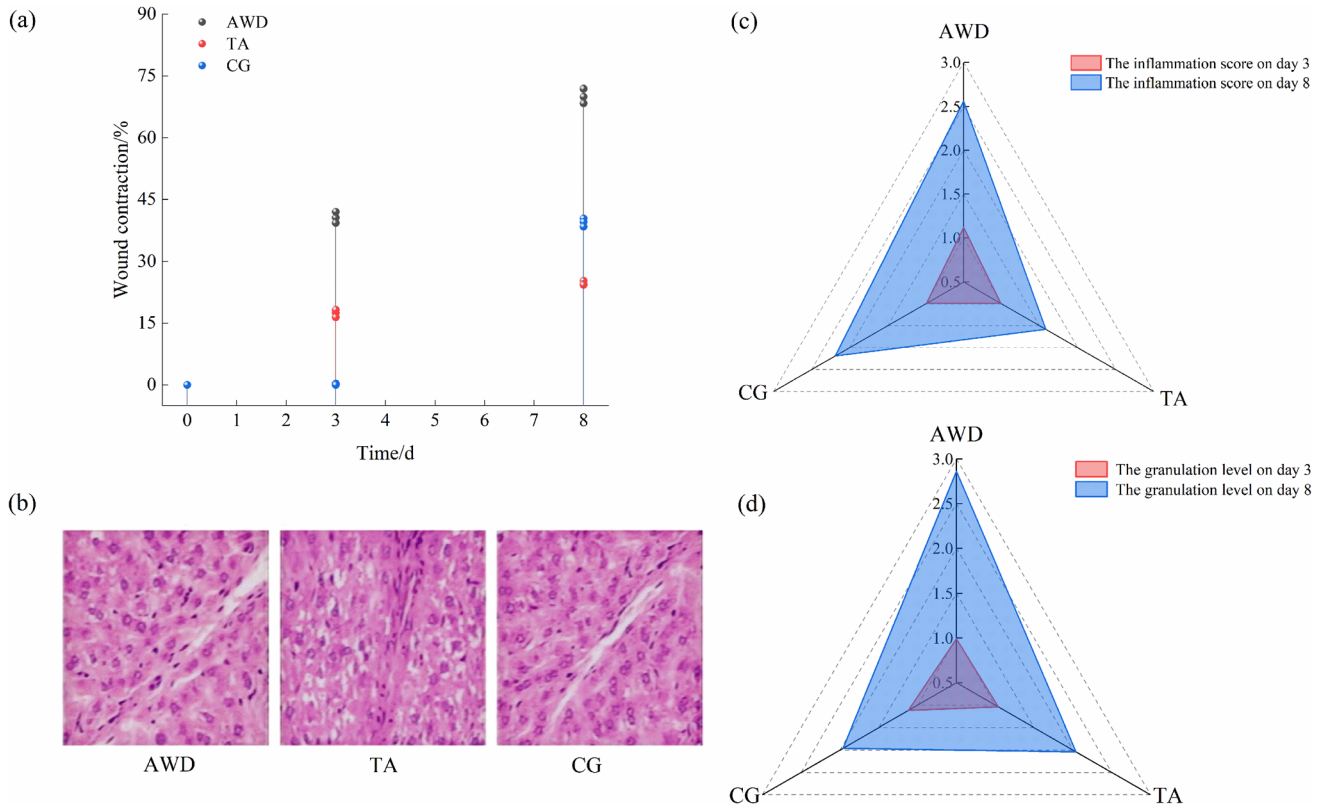

Fig. 7 Comparison of wound contraction ability of various materials in mice. (a) Demonstrates the wound contraction rates of different groups at various time points (time/d). (b) Presents the histological sections of wound tissues from different groups on day 8. (c) and (d) Respectively show the inflammation scores and granulation tissue levels of different groups on day 3 and day 8.

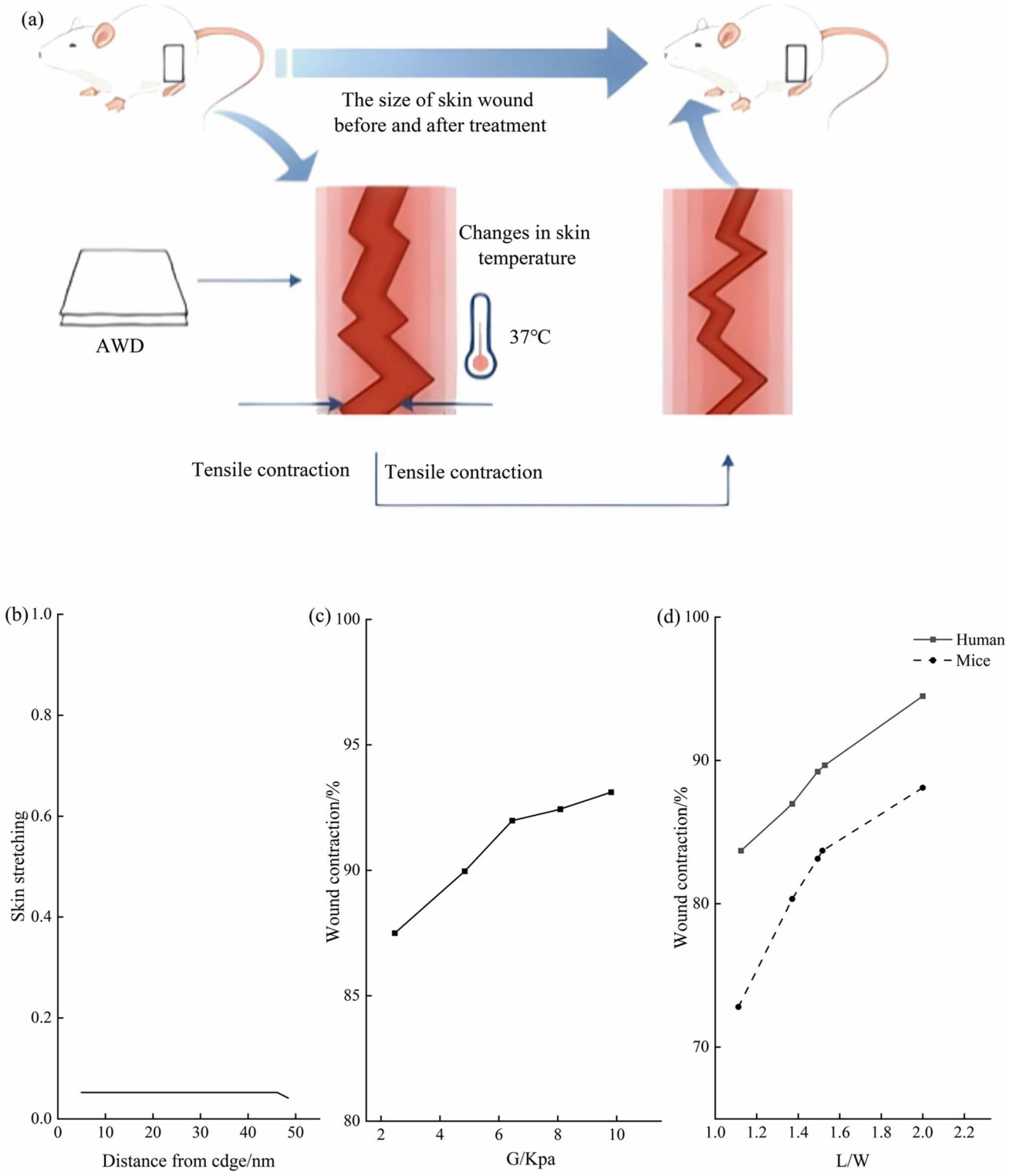

Fig. 8 Element simulation of add wound contraction analysis. (a) Schematic illustration of dynamic changes in wound size, skin temperature, and tensile contraction of the mouse skin wound model after AWD treatment; (b) curve of skin stretchability as a function of distance from the wound edge; (c) curve of wound contraction ratio *versus* G value; (d) curve of simulated wound contraction ratio for human-mouse models *versus* length-to-width ratio (L/W), where the initial wound model's width, length, thickness, and shear force are denoted by W, L, T, and G, respectively.

disorganized fibroblast alignment, persistent inflammatory cell accumulation, and sparse epithelial coverage (≤30% and ≤25% of the wound area, respectively). Quantitative analyses of inflammatory cell infiltration and granulation tissue formation (Fig. 7c, d and SI Table S11) further demonstrated that AWD promoted granulation tissue development and wound epithelial

regeneration without severe inflammatory responses: the Day 8 inflammation score of the AWD group (1.2 ± 0.4) was significantly lower than that of TA (2.5 ± 0.6), PF (2.1 ± 0.5), CHD (1.8 ± 0.5), and CG (2.8 ± 0.7) (all $p < 0.05$), while its granulation tissue score (3.5 ± 0.5) was significantly higher than that of TA (2.1 ± 0.4), PF (2.4 ± 0.5), CHD (2.8 ± 0.6), and CG (2.0 ± 0.4) (all $p < 0.05$). Collectively, these findings illustrate that AWD synergistically enhances wound healing quality at multiple levels, including accelerating contraction, regulating inflammation, and promoting tissue regeneration.

3.13 Finite element simulation of AWD-induced wound

The finite element simulation analysis diagram of AWD wound contraction is shown in Fig. 8, which is used to present the highly nonlinear thermosensitive response behavior of AWD and the influence of mechanical parameters on wound contraction. The skin is constructed as an Ogden hyperelastic material model, which can accurately capture the initial toe modulus and hardening effect of the skin when subjected to large tensile forces.[7] The finite element model is parameterized to characterize the mechanical properties of mouse skin and AWD, and the corresponding values are extracted to simulate the thermosensitive response behavior of PNIPAm. Fig. 8a intuitively presents the dynamic changes of AWD in treating mouse skin wounds. This schematic diagram clearly shows the correlation among wound size, skin temperature change, and tensile contraction before and after treatment. When AWD is in an environment of 37 °C, it contracts due to the thermosensitive effect, exerting a tensile force on the injured skin, causing limited displacement of the injured skin, and thus significantly promoting the healing of skin wounds. Simulation results show that when AWD contracts due to the thermosensitive effect, the injured skin produces limited displacement and tensile force, which significantly promotes skin wound healing (Fig. 8b). From the trend of the curve, it can be seen that with the increase of shear force, the wound contraction rate shows an upward trend. This indicates that appropriately increasing the shear force can effectively improve the contraction effect of AWD on wounds (Fig. 8c). Finite element models of human and mouse skin wounds were constructed, with the same initial wound parameters (such as width, length, AWD thickness, *etc.*) set, and the action process of AWD under the same thermosensitive conditions was simulated. With the increase of the length/width ratio, the wound contraction rates of both human and mouse models show an upward trend. The wound contraction rate of the mouse model is 75.28% (Fig. 8d and SI Table S12), which closely matches the experimental measurement of 68.67% within an acceptable error margin, fully verifying the reliability and accuracy of this finite element model (SI Table S8). Therefore, further based on this reliable model, the influence of material properties and geometric properties of AWD on wound contraction performance was studied in depth. Simulation prediction results show that with the increase of AWD modulus, the contraction force generated by it increases, thereby significantly improving the wound contraction effect; at the same time, the expansion of the bonding area between AWD and the skin can make the stress transmission more uniform, effectively reducing stress concentration, and further enhancing the wound contraction performance.

4 Discussion

4.1 Synergistic "temperature-mechanics" effect of PNIPAm phase transition and FSG ionic crosslinking for body temperature-triggered wound contraction

This study constructed an FSG-CS hybrid network *via* a cryogelation (4 °C) strategy, significantly enhancing the tensile strength and fracture energy of AWD. The performance improvement of AWD compared to single-network PNIPAm hydrogels can be attributed to the regulation of molecular chain crosslinking kinetics by low temperature, which delays the crosslinking rate between FSG and NIPAm to promote ordered arrangement of molecular chains and formation of a uniform hybrid network structure[23]—this mechanism is consistent with the low-temperature-induced gelatin network optimization proposed by Yu *et al.*[21] Additionally, AWD exhibits superior volume shrinkage rate and areal contraction tension at 37 °C relative to traditional materials like mussel-mimetic dressings, with AAm mediating active responses that generate tensile forces at wound edges to induce skin contraction.[5–7] This "temperature-mechanics" synergy originates from the coupling of PNIPAm phase transition properties with FSG ionic crosslinking networks, enabling body temperature-triggered wound contraction without external stimulation and providing an adaptive solution for dynamic wound repair. Compared with previous FSG-CS composite studies: Ranjbar *et al.*[11] prepared chitosan/gelatin sponges with hemostatic function but no thermoresponsive contraction; Diao *et al.*[4] developed pH/temperature co-responsive CS/NIPAM hydrogels but lacked finite element modeling for performance prediction and mechanical mechanism verification. This work fills these gaps by integrating thermoresponsive contraction, finite element optimization, and controlled Ag^+ release, providing a more comprehensive solution for intelligent wound repair. In contrast to the method reported by Zheng *et al.*[31] that achieves dynamic response through magnetic field-regulated hydrogel crosslinking—a technique requiring external stimulation and complex procedures—this study internally optimizes network structure *via* a cryogenic process, enabling high ductility without additional equipment in a simple and cost-effective manner.

4.2 AWD balances long-term antibacterial activity and biocompatibility *via* Ag^+ controlled-release strategy

The antibacterial efficacy of silver nanoparticles (AgNP) primarily relies on their nanoscale size effect and silver ion release.[13] Among these, AWD demonstrates stronger antibacterial capacity, attributed to the small size of AgNP enabling penetration of bacterial cell membranes, interaction with intracellular enzymes to inhibit their activity, and disruption of bacterial metabolic processes. Concurrently, slowly released silver ions (Ag^+) further bind to bacterial DNA to suppress replication.[27] Notably, no AgNP leakage was detected in release experiments, indicating that AWD achieves long-term antibacterial activity through sustained Ag^+ release to avoid potential toxicity from direct nanoparticle release. While

AgNP exhibit promising antibacterial efficacy, their biosafety remains a concern, as Pryjmaková *et al.*[26] showed that high-dose nano-silver injections may affect mouse internal organs, body weight, and tissue histology. In this study, *in vivo* experiments confirmed that AWD neither triggered significant inflammatory responses nor inhibited granulation tissue formation and epithelial regeneration. Furthermore, cell cytotoxicity tests showed >85% viability of NIH/3T3 and HaCaT cells exposed to 100% AWD extract, and ICP-MS results showed no significant Ag^+ accumulation in mouse liver and kidney. These results demonstrate that AWD's controlled-release strategy balances antibacterial efficacy and biocompatibility, providing a new paradigm for the regulated application of AgNP in wound repair. Similar to the regulatory effect of UVC-GA on intestinal microbiota[35]—a modified bioactive substance that promotes the growth of beneficial bacteria (*e.g.*, *Bifidobacterium longum*, *Lactobacillus plantarum*) and inhibits harmful bacteria (*e.g.*, *Klebsiella pneumoniae*)—AWD's Ag^+ controlled release not only exerts targeted antibacterial activity but also avoids disrupting the host's microbial homeostasis, which is crucial for long-term *in vivo* safety.

4.3 Synergistic construction of dual networks *via* covalent-ionic crosslinking enables order-of-magnitude enhancement of AWD toughness

The matrix toughness of 2M AWD is enhanced by orders of magnitude compared to single-network systems through the synergistic construction of dual networks *via* covalent crosslinking (MBAA-PNIPAm) and ionic crosslinking (Ca^{2+}-FSG), which originates from the energy dissipation mechanism of the bilayer network: the covalent crosslinking network absorbs energy through chain breaking, whereas the ionic crosslinking network dissipates energy *via* reversible bond recombination. This dual-network design enables synergistic interactions where the covalently crosslinked PNIPAm network bridges crack tips in the matrix to maintain overall structural integrity, while the ionically crosslinked FSG network consumes energy under deformation.[32] Given the same concentration of covalent crosslinkers, increasing NIPAm monomer content extends the chain length of PNIPAm between two covalent crosslinks, thereby enhancing crack bridging effects and fracture energy—findings consistent with other bilayer network hydrogels.[27] Compared to single-network SA and SN, AWD demonstrates significant advantages in adhesion energy, indicating that the multi-scale adhesion sites (electrostatic interactions, hydrogen bonds, *etc.*) provided by its hybrid network are better adapted to the demands of complex physiological environments.[12] This design strategy effectively addresses the bottleneck of insufficient mechanical properties in traditional gelatin materials, expanding research directions for the high-value utilization of marine biological resources.

4.4 Integrating Ogden–Flory theory to construct AWD contraction model and elucidate mechanisms of modulus-enhanced stress transfer and adhesion surface homogenization damage reduction

This study constructed a quantitative correlation model between AWD contraction behavior and skin mechanical response by integrating the Ogden hyperelastic model with Flory–Rehner thermodynamic theory, where simulation analysis showed that the error between wound displacement caused by AWD contraction and experimental measurements was only 6.61%, thereby validating the model's reliability. The model details include: (1) constitutive equations: modified Flory–Rehner model for AWD thermoresponsiveness, Ogden model for skin; (2) parameters: $\chi = 0.52$, $N = 1000$, $\alpha_1 = 10$ Pa, $\alpha_2 = 110$ Pa; (3) element type: CPE8RH; (4) boundary conditions: skin left/right edges fully constrained, bottom edge fixed horizontally; (5) thermoresponsive implementation: UHYPER subroutine simulating volume shrinkage at 37 °C. Mesh convergence test confirmed that 1 mm mesh size balances accuracy and efficiency. The model further elucidates that an increase in AWD modulus enhances the transmission efficiency of contraction stress, while an expanded adhesive area facilitates stress distribution homogenization to reduce secondary damage caused by local stress concentration.[7] However, the current model has not incorporated the feedback effect of extracellular matrix remodeling on the mechanical environment, and future research should further optimize the model through multi-physics field coupling methods (such as cell–matrix interactions).[33,34]

4.5 Critical role of physicochemical characterization in validating AWD performance

The physicochemical characterizations (FTIR, DSC/TGA, swelling behavior, WVTR, and degradation test) in this study comprehensively validated the rationality of AWD's structure and the adaptability of its functions. FTIR analysis directly confirmed the construction of the covalent-ionic-hydrogen bond synergistic crosslinked network, providing a structural basis for the material's mechanical properties and thermosensitive response; the LCST (32.5 ± 0.8 °C) determined by DSC ensures the material's rapid response ability in the physiological environment; the synergistic optimization of swelling behavior and WVTR solves the problem of "imbalanced moisturizing and drainage" of traditional dressings; the controlled degradation rate guarantees the safety and functional sustainability of the material *in vivo*. In addition, the statistical analysis of SEM pore structure reveals the correlation between the material's microstructure and macro-mechanical properties, providing a quantitative basis for subsequent material optimization. The supplementation of these characterization data makes the performance evaluation of AWD more comprehensive and reliable, meeting the rigor requirements of biomaterial research.

5 Conclusions

This study successfully developed a temperature-responsive active wound dressing (AWD) using fish skin gelatin (FSG) and chitosan (CS) as matrices *via* a synergistic strategy of low-temperature gelation and covalent-ionic crosslinking. Compared with previous FSG-CS composites, this work innovates in three aspects: (1) "PNIPAm-FSG" synergy for body temperature-triggered contraction without external stimulation; (2) controlled Ag^+ release balancing antibacterial activity and biocompatibility; (3) finite element model based on Ogden–Flory theory for quantitative prediction of wound contraction. The AWD exhibited outstanding

mechanical properties, including a tensile strength of 600.05% and fracture energy of 2000.47 J m^{-2} at 4 °C, along with a 22.17% volume shrinkage ratio at 37 °C within 3 h. Furthermore, it demonstrated significant antibacterial activity and promoted wound contraction by 45.28% in mice, validating its efficacy in wound healing. The "temperature-mechanics" synergistic regulation strategy integrates the thermosensitive property of FSG with the cationic antibacterial activity of CS to achieve autonomous body temperature response. At the same time, the introduction of silver nanoparticles and finite element modeling to overcome the functional limitations of traditional dressings, providing a new paradigm for intelligent biomaterial design. Scientific contributions include elucidating the wound healing mechanism *via* mechanical force-induced collagen orientation and verifying the excellent biocompatibility of AWD. Practically, AWD enables high-value utilization of aquatic by-products, reducing production costs, and offers an adaptive solution for complex wound repair without external stimulation. Future research may focus on exploring the shrinkage mechanism of AWD in low-temperature environments to expand its application in cold-region trauma repair, and optimizing the mechanical adaptability between the dressing and skin *via* multi-physics coupling models to facilitate clinical translation. This study establishes a theoretical foundation for the high-value application of fish skin gelatin and chitosan in wound repair, paving the way for the precision development of intelligent wound dressings.

Ethical statement

All animal experiments were conducted in accordance with the guidelines for the care and use of laboratory animals approved by the Guangxi Academy of Fishery Science Animal Ethics Committee (approval no. GAFS-2024-08). Every effort was made to minimize animal suffering and reduce the number of animals used.

Conflicts of interest

The authors have no conflict of interest to declare.

Data availability

The data supporting the findings of this study are included as part of the Supplementary Information.

Supplementary information: 8 supplementary figures (covering material preparation schematics, characterization data, performance tests, and wound healing mechanism diagrams) and 12 supplementary tables (containing experimental parameters, test results, and evaluation criteria). See DOI: https://doi.org/10.1039/d5ra05902j.

Acknowledgements

This work was supported by the Guangxi Natural Science Foundation (2024JJB130305), and Zhoushan Municipal Science and Technology Bureau project (2022C31064).

References

1 T. LópezGoerne, A. Arévalo and F. J. PadillaGodínez, Effect of catalytic nanomedicine on amputation-stage chronic venous ulcers: four case studies, *Wound Management Prev.*, 2023, **69**(4), 18–24, DOI: 10.25270/wmp.23010.

2 H. Chen, R. Zhang, G. Zhang, *et al.*, Naturally inspired tree-ring structured dressing provides sustained wound tightening and accelerates closure, *Adv. Mater.*, 2025, **37**(3), e2410845, DOI: 10.1002/adma.202410845.

3 K. Guo, K. Ou, Md. A. A. Newton, *et al.*, Multifunctional Janus nanofibrous membrane with unidirectional water transport and pH-responsive color-changing for wound dressing, *J. Colloid Interface Sci.*, 2025, **679**(Pt B), 723–736, DOI: 10.1016/j.jcis.2024.10.137.

4 J. Diao, Y. Meng, L. Wang, *et al.*, Temperature/pH Co-responsive CS/NIPAM-Based hydrogel with controlled release of Ga^{3+} for improved infected wound healing, *Chem. Eng. Sci.*, 2024, **294**, 120104, DOI: 10.1016/j.ces.2024.120104.

5 Y. Zhao, J. Kang, Y. Cui, *et al.*, Mechanically tunable, antibacterial and bioactive mussel adhesive protein/hyaluronic acid coacervates as bioadhesives, *Int. J. Biol. Macromol.*, 2023, **247**, 125773, DOI: 10.1016/j.ijbiomac.2023.125773.

6 Y. Liu, H. Wang, J. Li, *et al.*, Gecko-Inspired Controllable Adhesive: Structure, Fabrication, and Application, *Biomimetics*, 2024, **9**(3), 149, DOI: 10.3390/biomimetics9030149.

7 B. Chen, D. Zhu, Q. Li, *et al.*, Mechanically Reinforced and Injectable Universal Adhesive Based on a PEI-PAA/Alg Dual-Network Hydrogel Designed by Topological Entanglement and Catechol Chemistry, *ACS Appl. Mater. Interfaces*, 2023, **15**(51), 59826–59837, DOI: 10.1021/acsami.3c14743.

8 B. Zhang, L. Jia, J. Jiang, *et al.*, Biomimetic Microstructured Hydrogels with Thermal-Triggered Switchable Underwater Adhesion and Stable Antiswelling Property, *ACS Appl. Mater. Interfaces*, 2021, **13**(30), 36574–36586, DOI: 10.1021/acsami.1c10051.

9 W. Zhang, L. Liu, H. Cheng, *et al.*, Hydrogel-based dressings designed to facilitate wound healing, *Mater. Adv.*, 2024, **5**, 1364–1394, DOI: 10.1039/D3MA00682D.

10 H. Cao, J. Wang, Z. Y. Hao, *et al.*, Gelatin-based biomaterials and gelatin as an additive for chronic wound repair, *Front. Pharmacol*, 2024, **15**, 1398939, DOI: 10.3389/fphar.2024.1398939.

11 J. Ranjbar, M. Koosha, H. Chi, *et al.*, Novel Chitosan/Gelatin/Oxidized Cellulose Sponges as Absorbable Hemostatic Agents, *Cellulose*, 2021, **28**, 3663–3675, DOI: 10.1007/s10570-021-03699-9.

12 M. A. Matica, F. L. Aachmann, A. Tøndervik, *et al.*, Chitosan as a Wound Dressing Starting Material: Antimicrobial Properties and Mode of Action, *Int. J. Mol. Sci.*, 2019, **20**(23), 5889, DOI: 10.3390/ijms20235889.

13 P. Kazimierczak, M. Koziol and A. Przekora, The Chitosan/Agarose/NanoHA Bone Scaffold-Induced M2 Macrophage

Polarization and Its Effect on Osteogenic Differentiation In Vitro, *Int. J. Mol. Sci.*, 2021, **22**(3), 1109, DOI: 10.3390/ijms22031109.

14 K. E. Rothenberg and R. Fernandez-Gonzalez, Forceful Closure: Cytoskeletal Networks in Embryonic Wound Repair, *Mol. Biol. Cell*, 2019, **30**(12), 1353–1358, DOI: 10.1091/mbc.E18-04-0248.

15 J.-L. Yin, Y. Wu, Z.-W. Yuan, *et al.*, Advances in Scarless Foetal Wound Healing and Prospects for Scar Reduction in Adults, *Cell Proliferation*, 2020, **53**(11), e12916, DOI: 10.1111/cpr.12916.

16 L. Hao, J. Li, P. Wang, *et al.*, Spatiotemporal Magnetocaloric Microenvironment for Guiding the Fate of Biodegradable Polymer Implants, *Adv. Funct. Mater.*, 2021, **31**(15), 2009661, DOI: 10.1002/adfm.202009661.

17 A. Botter, M. Beltrandi, G. L. Cerone, *et al.*, Development and testing of acoustically - matched hydrogel - based electrodes for simultaneous EMG - ultrasound detection, *Med. Eng. Phys.*, 2019, **64**, 74–79, DOI: 10.1016/j.medengphy.2018.12.002.

18 S. Cheng, C. Zhang, J. Li, *et al.*, Highly efficient removal of antibiotic from biomedical wastewater using Fenton-like catalyst magnetic pullulan hydrogels, *Carbohydr. Polym.*, 2021, **262**, 117951–117959, DOI: 10.1016/j.carbpol.2021.117951.

19 Y. Yang, J. Wang, S. Huang, *et al.*, Bacteria-responsive programmed self-activating antibacterial hydrogel to remodel regeneration microenvironment for infected wound healing, *Natl. Sci. Rev.*, 2024, **11**(4), nwae044, DOI: 10.1093/nsr/nwae044.

20 Y. Wang, G. Xia, H. Yu, *et al.*, Mussel-Inspired Design of a Self-Adhesive Agent for Durable Moisture Management and Bacterial Inhibition on PET Fabric, *Adv. Mater.*, 2021, **33**(35), e2100140, DOI: 10.1002/adma.202100140.

21 E. Yu, C. Pan, X. Luo, *et al.*, Structural characteristics, component interactions and functional properties of gelatins from three fish skins extracted by five methods, *Int. J. Biol. Macromol.*, 2023, **248**, 125813, DOI: 10.1016/j.ijbiomac.2023.125813.

22 N. Kahya, A. Kartun, I. N. Korkut, *et al.*, Silver Nanowire-Coated Porous Alginate Films for Wound Dressing Applications: Antibacterial Activity, Cell Proliferation, and Physical Characterization, *ACS Omega*, 2024, **9**(50), 49032–49042, DOI: 10.1021/acsomega.4c02467.

23 J. Heeseok, L. Deuk Yong, Y. Dae Hyeok, *et al.*, Mechanical and Cell-Adhesive Properties of Gelatin/Polyvinyl Alcohol Hydrogels and Their Application in Wound Dressing, *Macromol. Res.*, 2022, **30**(4), 223–229, DOI: 10.1007/S13233-022-0027-7.

24 (*a*) J. L. Wang, J. H. Wei, S. H. Su, *et al.*, Thermal-recoverable tough hydrogels enhanced by porphyrin decorated graphene oxide, *Nanomaterials*, 2019, **9**(10), 1487; (*b*) J. Wang, J. Wei, S. Su, *et al.*, Thermal-Recoverable Tough Hydrogels Enhanced by Porphyrin Decorated Graphene Oxide, *Nanomaterials*, 2019, **9**(10), 1487, DOI: 10.3390/nano9101487.

25 R. Su, S. Ge, H. Li, *et al.*, Synchronous synthesis of Cu2O/Cu/rGO@carbon nanomaterials photocatalysts via the sodium alginate hydrogel template method for visible light photocatalytic degradation, *Sci. Total Environ.*, 2019, **693**, 133657, DOI: 10.1016/j.scitotenv.2019.133657.

26 J. Pryjmaková, D. Grossberger, A. Kutová, *et al.*, A New Promising Material for Biological Applications: Multilevel Physical Modification of AgNP-Decorated PEEK, *Nanomaterials*, 2023, **13**(24), 3079, DOI: 10.3390/nano13243079.

27 Z.-H. Hu, A. M. Omer, X.-K. Ouyang, *et al.*, Fabrication of carboxylated cellulose nanocrystal/sodium alginate hydrogel beads for adsorption of Pb(II) from aqueous solution, *Int. J. Biol. Macromol.*, 2018, **108**, 149–157, DOI: 10.1016/j.ijbiomac.2017.11.171.

28 I. P. S. Fernando, T. U. Jayawardena, H.-S. Kim, *et al.*, A keratinocyte and integrated fibroblast culture model for studying particulate matter-induced skin lesions and therapeutic intervention of fucosterol, *Life Sci.*, 2019, **233**, 116714, DOI: 10.1016/j.lfs.2019.116714.

29 Z. Li, J. Huang, Y. Jiang, *et al.*, Novel Temperature - Sensitive Hydrogel Promotes Wound Healing Through YAP and MEK - Mediated Mechanosensitivity, *Adv. Healthcare Mater.*, 2022, **11**(23), e2201878, DOI: 10.1002/adhm.202201878.

30 Y. Li, K. Mei, Y. Wang, *et al.*, Finite element model analysis of long-term performance of composite anchorage based on double-material parameters, *J. Build. Eng.*, 2024, **87**, 109059, DOI: 10.1016/j.jobe.2024.109059.

31 X. Zheng, Y. Chen, N. Dan, *et al.*, Highly stable collagen scaffolds crosslinked with an epoxidized natural polysaccharide for wound healing, *Int. J. Biol. Macromol.*, 2021, **182**, 1994–2002, DOI: 10.1016/j.ijbiomac.2021.05.189.

32 X. Y. Lee, H. W. Fan and H. J. Koh, Characterization of electrically conductive hydrogels-polyaniline/polyacrylamide and graphene/polyacrylamide, *Mater. Sci. Forum*, 2020, **977**, 59–64, DOI: 10.4028/www.scientific.net/msf.977.59.

33 J. Wang, J. Wei, S. Su, *et al.*, Thermal-Recoverable Tough Hydrogels Enhanced by Porphyrin Decorated Graphene Oxide, *Nanomaterials*, 2019, **9**(10), 1487, DOI: 10.3390/nano9101487.

34 M. Wu, Z. Lu, K. Wu, *et al.*, Recent advances in the development of nitric oxide-releasing biomaterials and their application potentials in chronic wound healing, *J. Mater. Chem. B*, 2021, **9**(35), 7063–7075, DOI: 10.1039/d1tb00847a.

35 X. Luo, G. Z. Jiang, Z. D. Ruan, *et al.*, Effect of ultraviolet-irradiated modified gallic acid (UVC-GA) on the intestinal microbiota of mice, *Food Wellness*, 2026, **2**, 100035, DOI: 10.1016/j.foodw.2025.100035.